Impact of ionizing radiation on superconducting qubit coherence

Antti P. Vepsäläinen[1,*], Amir H. Karamlou[1], John L. Orrell[2,], Akshunna S. Dogra[1,4], Ben Loer[2], Francisca Vasconcelos[1], David K. Kim[3], Alexander J. Melville[3], Bethany M. Niedzielski[3], Jonilyn L. Yoder[3], Simon Gustavsson[1], Joseph A. Formaggio[1], Brent A. VanDevender[2], and William D. Oliver[1,3]**

[1]Massachusetts Institute of Technology, Cambridge, MA 02139, USA
[2]Pacific Northwest National Laboratory, Richland, WA 99352, USA
[3]MIT Lincoln Laboratory, Lexington, MA 02421, USA
[4]Harvard University, Cambridge, MA 02138, USA
[*]Corresponding author for qubit operations: avepsala@mit.edu
[**]Corresponding author for radiation exposure: john.orrell@pnnl.gov

arXiv:2001.09190v1 [quant-ph] 24 Jan 2020

The practical viability of any qubit technology stands on long coherence times and high-fidelity operations[1], with the superconducting qubit modality being a leading example[2,3]. However, superconducting qubit coherence is impacted by broken Cooper pairs,[4–6] referred to as quasiparticles, with a density that is empirically observed to be orders of magnitude greater than the value predicted for thermal equilibrium by the Bardeen-Cooper-Schrieffer (BCS) theory of superconductivity[7–9]. Previous work[10–12] has shown that infrared photons significantly increase the quasiparticle density, yet even in the best isolated systems, it still remains higher[10] than expected, suggesting that another generation mechanism exists. In this Letter, we provide evidence that ionizing radiation from environmental radioactive materials and cosmic rays contributes to this observed difference, leading to an elevated quasiparticle density that would ultimately limit superconducting qubits of the type measured here to coherence times in the millisecond regime. We further demonstrate that introducing radiation shielding reduces the flux of ionizing radiation and positively correlates with increased coherence time. Albeit a small effect for today's qubits, reducing or otherwise mitigating the impact of ionizing radiation will be critical for realizing fault-tolerant superconducting quantum computers.

Over the past 20 years, superconducting qubit coherence times have increased more than five orders of magnitude due to improvements in device design, fabrication, and materials, from less than one nanosecond in 1999[13] to more than 100 µs in contemporary devices[14,15]. Nonetheless, to realize the full promise of quantum computing, far longer coherence times will be needed to achieve the operational fidelities required for fault-tolerance[16].

Today, the performance of superconducting qubits is limited in part by quasiparticles - a phenomenon known colloquially as "quasiparticle poisoning." Although it was recently suggested that high-energy cosmic rays result in bursts of quasiparticles that reduce the quality factor in superconducting granular aluminum resonators[17], to date there has been no quantitative model or experimental validation of the effect of environmental ionizing radiation on superconducting qubits.

In this work, we measure the impact of environmental radiation on superconducting qubit performance. We develop a model and determine its parameters by measuring the effect of radiation from a calibrated radioactive source on qubit coherence. We use this model to infer the energy-relaxation rate $\Gamma_1 \approx 1/4\,\mathrm{ms}^{-1}$ for our qubit if it were limited solely by the measured level of naturally occurring cosmic rays and background environmental radiation present in our laboratory. We then demonstrate that the deleterious effects of this external radiation can be reduced by protecting the device with a lead shield. The improvement in qubit coherence from this independent shielding measurement is consistent with the radiation-limited Γ_1 inferred from the model. Furthermore, we show that our estimate of the quasiparticle density due solely to the ionizing radiation agrees with the observed surplus quasiparticle density in qubits that are well-isolated from thermal photons[7,10]. This finding is of crucial importance for all superconducting applications in which quasiparticle excitations are harmful, such as superconducting quantum computing or Majorana fermion physics[18].

For emerging quantum processors, one of most commonly used modalities is the superconducting transmon qubit[19], which comprises one or more Josephson junctions and a shunt capacitor. The intrinsic nonlinear inductance of the junction in combination with the linear capacitance forms an anharmonic oscillator[20]. The non-degenerate transition energies of such an oscillator are uniquely addressable, and in particular, its ground and first excited states serve as the logical $|0\rangle$ and $|1\rangle$ states of the qubit, respectively. In an ideal situation, qubits would suffer no loss of coherence during the the run-time of a quantum computation. However, interactions with the environment introduce decoherence channels, which for the case of energy decay, result in a loss of qubit polarization over

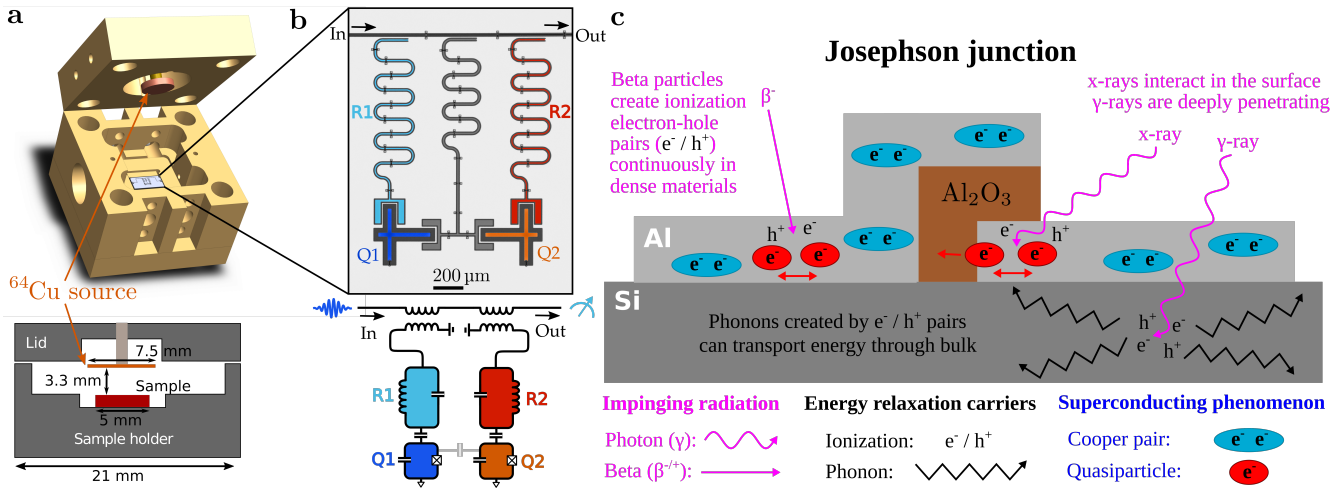

Figure 1. Schematic of the experiment. a) Illustration of the sample holder and the ^{64}Cu radiation source. The source is mounted 3.3 mm above the silicon chip containing the superconducting aluminum transmon qubits. b) False-color micrograph and circuit schematic of the qubit sample. The sample consists of two transmon qubits, Q1 (blue, left) and Q2 (orange, right). The resonators used to readout the qubits are shown with red and cyan. The resonators are inductively coupled to a common microwave transmission line, through which both qubit control and readout pulses are sent. The control pulses and the measurement pulses are generated using microwave sources and arbitrary waveform generators at room temperature (not shown, see Supplementary material). c) Diagram of the possible quasiparticle generation processes. Incoming ionizing radiation (from $\beta^{\pm}$ and γ particles) interact with the Al qubit and Si substrate, creating electron-hole pairs due to the ionization of atoms and phonons (see text). The subsequent energy cascade of these particles ultimately breaks Cooper pairs and thereby generates quasiparticles.

time,

$$p(t) = \mathrm{e}^{-\Gamma_1 t}, \tag{1}$$

where $p(t)$ is the excited-state probability and $\Gamma_1 \equiv \frac{1}{T_1}$ is the energy relaxation rate corresponding to the relaxation time T_1, which limits the qubit coherence time. For such processes, the total energy relaxation rate is a combination of all the individual rates affecting the qubit,

$$\Gamma_1 = \Gamma_{\mathrm{qp}} + \Gamma_{\mathrm{other}}, \tag{2}$$

where Γ_{qp} is the energy relaxation rate due to the quasiparticles and Γ_{other} contains all the other loss channels, such as radiation losses, dielectric losses and the effect of two-level fluctuators in the materials[21]. In the transmon, the quasiparticle energy-relaxation rate Γ_{qp} depends on the normalized quasiparticle density $x_{\mathrm{qp}} = n_{\mathrm{qp}}/n_{\mathrm{cp}}$ and the frequency of the qubit ω_q, such that[22]

$$\Gamma_{\mathrm{qp}} = \sqrt{\frac{2\omega_q \Delta}{\pi^2 \hbar}} x_{\mathrm{qp}}. \tag{3}$$

The Cooper pair density (n_{cp}) and the superconducting gap (Δ) are material-dependent parameters, and for thin-film aluminum they are $n_{\mathrm{cp}} \approx 4 \times 10^6\,\mu\mathrm{m}^{-3}$ and $\Delta \approx 180\,\mu\mathrm{eV}$. This relation allows us to use the coherence of a transmon as a sensor for quasiparticle density in the superconductor as well as to estimate the maximum coherence time of a transmon given a certain quasiparticle density. The thermal equilibrium contribution to x_{qp} is vanishingly small at the effective temperature of the sample, $T_{\mathrm{eff}} \approx 40\,\mathrm{mK}$, compared with the other generation mechanisms we shall consider here.

Currently, there exists no quantitative microscopic model directly connecting interactions of ionizing radiation (*e.g.*, betas, gammas, x-rays, etc.) to quasiparticle populations in superconductors. However, a phenomonological picture describing the processes involved in this connection is shown in Fig. 1c. The energy of ionizing radiation absorbed in the aluminum metal and silicon substrate is initially converted into ionization electron-hole pairs. We purposefully distinguish these high-energy excitations due to the ionization of atoms – which occur in both aluminum and silicon – from the lower-energy quasiparticle excitations resulting from broken Cooper-pairs in aluminum. Thereafter, a non-equilibirum relaxation cascade involving secondary ionization carrier and phonon production serves to transfer the absorbed radiation power to and within the aluminum qubit, where it breaks Cooper pairs and generates quasiparticles.

To estimate the effect of the radiation intensity measured in the laboratory, we employ a radiation transport simulations (see Methods for details) to calculate the quasiparticle generating power density P_{tot} close to the qubit, and use a simple model for quasiparticle dynamics[22]

$$\dot{x}_{\mathrm{qp}}(t) = -r x_{\mathrm{qp}}^2(t) - s x_{\mathrm{qp}}(t) + g, \tag{4}$$

where g is the quasiparticle generation rate, which linearly

depends on P_{tot}, r is recombination rate, and s is quasiparticle trapping rate. A steady state solution for the quasiparticle density is given by $x_{\mathrm{qp}} = (-s + \sqrt{s^2 + 4rg})/2r$, and if quasiparticle trapping is neglected ($s = 0$) then $x_{\mathrm{qp}} = \sqrt{g/r}$. In a separate quasiparticle injection experiment we verified that this is a valid approximation in our devices, see Supplementary material for discussion. By substituting the model for x_{qp} into Eq. (3) and using Eq. (2), the qubit decay rate is given by

$$\Gamma_1 = a\sqrt{\omega_{\mathrm{q}} P_{\mathrm{tot}}} + \Gamma_{\mathrm{other}}, \tag{5}$$

where a is an unknown coefficient accounting for conversion from absorbed power to quasiparticle generation rate and all the other constants. The value of a can be experimentally determined by exposing the qubit to a known source of ionizing radiation.

Results

Radiation exposure experiment

To quantify the effect of ionizing radiation on superconducting qubits and to measure the coefficient a in Eq. (5), we inserted a ^{64}Cu radiation source close to a sample containing two transmon qubits, Q1 and Q2, with average energy-relaxation rates of $\Gamma_1^{(\mathrm{Q1})} = 1/40\,\mu\mathrm{s}^{-1}$ and $\Gamma_1^{(\mathrm{Q2})} = 1/32\,\mu\mathrm{s}^{-1}$, and transition frequencies $\omega_{\mathrm{q}}^{(\mathrm{Q1})} = 2\pi \times 3.48\,\mathrm{GHz}$ and $\omega_{\mathrm{q}}^{(\mathrm{Q2})} = 2\pi \times 4.6\,\mathrm{GHz}$, see Figs. 1a and 1c. ^{64}Cu has a short half-life of 12.7 h, which permits an observation of the transition from elevated ionizing radiation exposure to normal operation conditions within a single cooldown of the dilution refrigerator. ^{64}Cu was produced by irradiating high-purity copper foil in the MIT Nuclear Reactor Laboratory (see Methods for details).

The energy relaxation rate Γ_1 of both qubits was repeatedly measured for over 400 hours during the radioactive decay of the ^{64}Cu source (see Fig. 2a and Supplementary materials). During this interval of time, the energy relaxation rate $\Gamma_1^{(\mathrm{Q1})}$ of Q1 decreased from $1/5.7\,\mu\mathrm{s}^{-1}$ to $1/35\,\mu\mathrm{s}^{-1}$ due to the gradually decreasing radioactivity of the source, and similarly for Q2. The half-life was long enough to measure individual Γ_1 values at essentially constant levels of radioactivity, yet short enough to sample Γ_1 over a wide range of radiation powers, down to almost the external background level. In addition to affecting qubit coherence, the resonance frequencies ω_{r} of the readout resonators shifted due to quasiparticle-induced changes in their kinetic inductance, consistent with the quasiparticle recombination model of Eq. (4) (see Supplementary material).

The intensity of the radiation source used in the experiment was calibrated as a function of time using the gamma-ray spectroscopy of a reference copper foil that had been irradiated concurrently. The foils included a small amount of longer-lived radioactive impurities that began to noticeably alter the radiated power density expected for ^{64}Cu about 180 hours

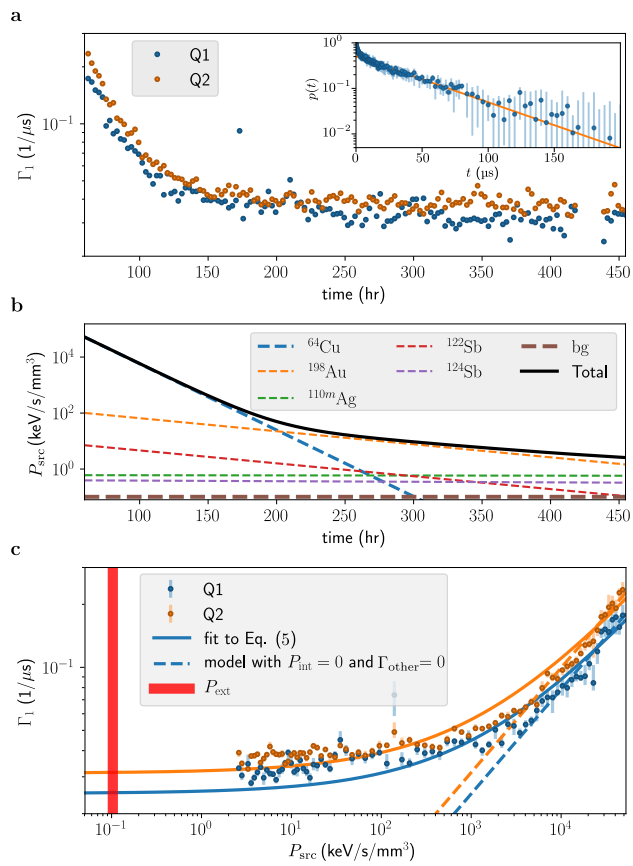

Figure 2. ^{64}Cu radiation exposure experiment. a) Measured energy relaxation rates $\Gamma_1 = 1/T_1$ of qubits Q1 (blue) and Q2 (orange) as a function of time when exposed to the ^{64}Cu source. The inset shows an example of the raw data used for fitting the energy relaxation rates. Blue points are the median of 20 measured qubit excited-state populations $p(t)$ at various times after the excitation pulse. Blue bars indicate the 95% confidence interval for the median. The orange line is the exponential fit to the data, given in Eq. (1). b) Power density of the radiation during the experiment derived from radiation transport simulations (see text). c) Energy relaxation rates Γ_1 as a function of radiation power density. The solid lines show the fit to the model of Eq. (4). The dashed lines show the fit to model of Eq. (4) with $\Gamma_{\mathrm{other}} = 0$ and $P_{\mathrm{int}} = 0$. The vertical red line is the radiation power density level due to the external radiation P_{ext}.

into the measurements (see Fig. 2b). For both the ^{64}Cu and the long-lived impurities, the radiation intensities from the different isotopes were converted to a single ionizing radiation power density using the radiation transport simulation package Geant4[23,24] (see Methods for details). The contributions of the different isotopes (dashed lines) and the resulting net power density (solid line) of the radiation from the source, P_{src}, are shown in Fig. 2b over the measurement time window.

Using the data in Fig. 2b as a method for calibrated time-power conversion, the energy relaxation rates of qubits Q1 and Q2 are presented as a function of the radiation power density P_{src} (Fig. 2c). In the high-P_{src} limit (short times), the model of Eq. (5) can be fit to the data to extract the value for the conversion coefficient $a = 5.4 \times 10^{-3}\sqrt{\mathrm{mm}^3/\mathrm{keV}}$ by assuming $P_{\mathrm{tot}} \approx P_{\mathrm{src}}$ dominates all radiation sources that generate quasiparticles as well as all other decay channels. In the low-P_{src} limit (long times), the qubit coherence is limited predominantly by the decay rate Γ_{other} and, to a lesser extent, by the long-lived radioactive impurities in the foil.

Having determined the coefficient a in Eq. (5), we now remove the calibrated radiation source. In its absence, the total radiation power density that generates quasiparticles can be categorized into two terms, $P_{\mathrm{tot}} = P_{\mathrm{int}} + P_{\mathrm{ext}}$. The term P_{int} accounts for radiation power sources that are internal to the dilution refrigerator, such as infrared photons from higher temperature stages or radioactive impurities present during the manufacturing of the refrigerator components. P_{ext} is the external ionizing radiation source outside the dilution refrigerator whose influence on the qubits we attempt to determine in the shielded experiment described in the next section.

To estimate the contribution of external radiation power P_{ext} to the data shown in Fig. 2, we directly measured the γ-ray field present in the laboratory using a NaI radiation detector (see Fig. 3 for the measured energy spectrum). The spectrum was used to determine the radiation intensities from cosmic rays and naturally occurring radioactive isotopes in the laboratory. These measured gamma-ray intensities were then used in a Geant4 radiation transport simulation to estimate the total external power density $P_{\mathrm{ext}} = (0.10 \pm 0.02)\mathrm{keV\,mm^{-3}\,s^{-1}}$ deposited in the aluminum that constitutes the resonators and qubits. About 60% of the external radiation power density results from the radioactive decays within the concrete walls of the laboratory ($0.06\,\mathrm{keV\,mm^{-3}\,s^{-1}}$), with cosmic rays contributing the remaining 40% ($0.04\,\mathrm{keV\,mm^{-3}\,s^{-1}}$). This external power level is indicated with a vertical red band in Fig. 2c. Although statistical errors in the measured intensities are small, we find a combined systematic uncertainty of approximately 20%. The different sources' contributions to the total systematic uncertainty are detailed in the Methods section.

Using the model in Eq. (5) with the determined parameters for a and P_{ext} and the known qubit frequencies, the lower limit on the total energy relaxation rate due to the external radiation P_{ext} in the absence of all other energy-relaxation mechanisms is $\Gamma_1^{(\mathrm{Q1})} \approx 1/3950\,\mu\mathrm{s}^{-1}$ and $\Gamma_1^{(\mathrm{Q2})} \approx 1/3130\,\mu\mathrm{s}^{-1}$, corresponding to the dashed lines in Fig. 2c. These rates correspond to the point at which naturally occurring radiation from the laboratory would become the dominant limiting contributor to the qubit coherence. Although the effect on the coherence of today's qubits is not dominant, the ionizing radiation has to be considered when aiming for coherence times required for fault-tolerant quantum computing. The difference in energy relaxation rates between the qubits is due to their different transition frequencies, which affects the quasiparticle-induced energy-relaxation rate according to Eq. (3). We can furthermore apply Eq. (3) to estimate the quasiparticle density caused by the ionizing radiation background, giving $x_{\mathrm{qp}} \approx 7 \times 10^{-9}$, which agrees well with the lowest reported excess quasiparticle densities[10].

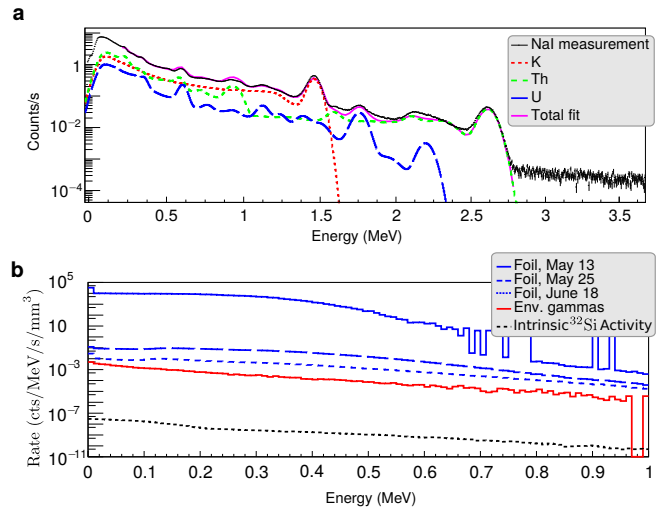

Figure 3. Environmental radioactivity assessment. a) Spectrum of radiation in the laboratory environment as measured by an unshielded NaI scintillation detector. The data is fit to the sum of spectra representing typical gamma fluxes from natural ^{238}U,^{232}Th, and ^{40}K contamination in concrete, convolved with a response function expected from a NaI detector. The resulting fit amplitudes give a total flux of around $\Phi \approx 1\,/\mathrm{cm}^2/\mathrm{s}/\mathrm{sr}$, consistent with typical values for concrete, see Table 2 in the Methods. b) Simulated spectrum of energy deposited in the substrate. The spectrum from the activated foil is shown at 3 different times: immediately after insertion, when emission is dominated by ^{64}Cu; after 12 days, when emission is dominated by ^{198}Au; and after 36 days, when emission is dominated by $^{110\mathrm{m}}$Ag. The estimate for environmental background is derived from the fit to the NaI measurement. ^{32}Si is a radioactive contaminant intrinsic to silicon, and represents the ultimate background level of radiation achievable if all other external radiation could be eliminated.[25]

Shielding experiment

We sought to verify the above result by shielding the qubits with 10 cm thick lead bricks outside the cryostat to reduce the external radiation and improve their coherence time, see Fig. 4. The shield was built on a scissor lift to be able to cyclically raise and lower it to perform an A/B test of its effect. By using the parameters extracted from the radiation exposure measurement and the model in Eq. (5), the expected improvement of the energy relaxation rate due to the shield

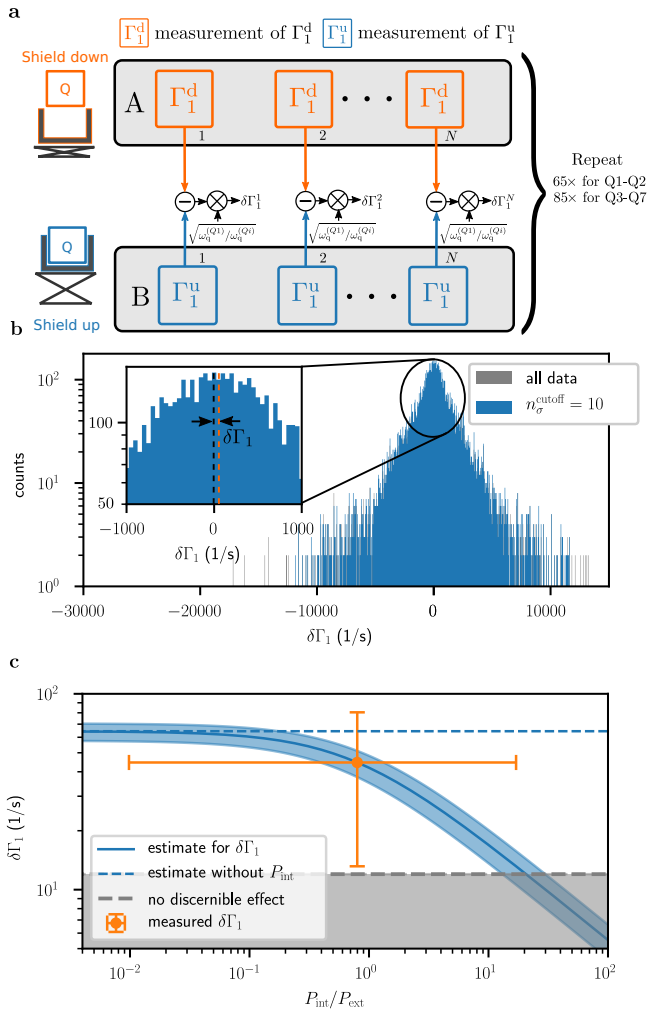

Figure 4. Qubit shielding experiment. a) Schematic of the shielding experiment. The energy relaxation rate of the qubits is measured N times with shield up, and then again N times with the shield down. This cycle is repeated 65 times for the sample with qubits Q1 and Q2 and 85 times for the sample with qubits Q3-Q7. b) Histogram of the differences in energy relaxation rates when the shield is up versus down. The inset shows the peak of the histogram. The orange vertical line shows location of the median of the distribution. Even though the median is small compared to the width of the distribution, it differs from zero in a statistically significant manner. c) Difference in the energy relaxation rates in the shielding experiment (orange dot) versus $P_{\mathrm{int}}/P_{\mathrm{ext}}$. Vertical error bars are the 95 % confidence intervals for the median of $\delta\Gamma_1$. Horizontal error bars are the corresponding confidence intervals for P_{int}. The blue line is the change in the energy relaxation rate estimated using the model from the ^{64}Cu radiation exposure measurement and Eq. (6). The filled blue area shows the confidence interval for the estimate assuming $\pm$ 20 % relative error for P_{ext}. Below the gray dashed line, the experiment is not sensitive enough to detect $\delta\Gamma_1$.

can be estimated from

$$\begin{aligned}\delta\Gamma_1 &\equiv \Gamma_1^{\mathrm{d}} - \Gamma_1^{\mathrm{u}} \\ &= a\sqrt{\omega_{\mathrm{q}}}\left(\sqrt{P_{\mathrm{int}} + (1-\eta^{\mathrm{d}})P_{\mathrm{ext}}} - \sqrt{P_{\mathrm{int}} + (1-\eta^{\mathrm{u}})P_{\mathrm{ext}}}\right) \\ &\simeq a\sqrt{\frac{\omega_{\mathrm{q}}}{P_{\mathrm{int}}}}\,\frac{(\eta^{\mathrm{u}} - \eta^{\mathrm{d}})}{2}P_{\mathrm{ext}}, \qquad (6)\end{aligned}$$

where η is the fraction of ionizing radiation blocked by the shield and the label u (d) corresponds to the parameters when the shield is up (down). The approximation in the last line is valid in the limit $P_{\mathrm{ext}} \ll P_{\mathrm{int}}$. We can make a realistic estimate of the efficiency of the shield by measuring the radiation energy spectrum with and without the shield using a NaI detector, giving $\eta^{\mathrm{u}} = 46.1\%$. Even when the shield is lowered, the qubits remain partially shielded from the bottom, resulting in $\eta^{\mathrm{d}} = 2.2\%$, see Methods for details. From Eq. (6), in the absence of internal radiation sources ($P_{\mathrm{int}} = 0$), the expected effect of the shield on the energy-relaxation rate of Q1 is $\delta\Gamma_1 \approx 1/15.5\,\mathrm{ms}^{-1}$, which is only 0.26 % of the energy-relaxation rate of qubit Q1.

To detect a signal this small, we measured the energy relaxation rates of the qubits while periodically placing the shield in the up and down positions and then comparing their difference over many cycles, similar in spirit to a Dicke switch radiometer "lock-in" measurement[26], see Fig 4a for a schematic. To speed up the data acquisition, we installed an additional sample in the dilution refrigerator with 5 qubits similar to Q1 and Q2.

Fig. 4b shows the histogram of the accumulated differences in the energy relaxation rates, $\delta\Gamma_1$, of all of the qubits over the entire measurement. The quasiparticle contribution to the energy relaxation rates of the qubits depends on their frequencies according to Eq. (5), and therefore we have normalized the changes in the energy relaxation rates to the frequency of Q1 by multiplying with a conversion factor $\sqrt{\omega_{\mathrm{q}}^{(Q1)}/\omega_{\mathrm{q}}^{(Qi)}}$. Even though reduced by the "lock-in" measurement, the distribution $\delta\Gamma_1$ has long tails due to the typical fluctuations and drifts in the energy relaxation rates of the qubits, observed in several experiments[21]. To reduce the effect of the fluctuations on the data analysis, we applied a cutoff at 10 standard deviations of the distribution. From the median of the histogram, we estimate the shift in the energy relaxation rate $\delta\Gamma_1 = 1/22.7\,\mathrm{ms}^{-1}$, 95% CI [1/75.8, 1/12.4] ms^{-1}. The Wilcoxon signed-rank test can be used to test if the measured energy-relaxation rates in the shield up and down positions differ, and yields a p-value of 0.006. As the p-value is much less than 0.05, we can reject the null hypothesis that the shield did not have any effect on the qubit coherence with high confidence, see Methods and the Supplementary material for additional details on the statistical analysis.

In Fig. 4c, we have compared the result of the shielding experiment to the estimate of the effect of the background radiation obtained from the radiation exposure measurement. The orange dot shows $\delta\Gamma_1$ extracted from the shielding ex-

periment. The solid blue line shows how this value would trend based on the predicted effect of the shield at the given P_{ext} measured in the laboratory for different values of internal radiation power density P_{int}. Although we do not know the exact value of P_{int}, we can approximate it by substituting the measured $\delta\Gamma_1$ and a into Eq. (6) and by solving for $P_{\text{int}} \approx 0.081\,\text{keV}\,\text{mm}^{-3}\,\text{s}^{-1}$, 95% CI [0, 1.73] $\text{keV}\,\text{mm}^{-3}\,\text{s}^{-1}$. This value for P_{int} corresponds to a total quasiparticle density $x_{\text{qp}} \approx 1.0 \times 10^{-8}$, again, consistent with earlier observations[7]. The observed low levels of P_{int} are achieved by shielding against infrared radiation inside the fridge as well as carefully filtering the connected control lines, see Supplementary material for the diagram of the measurement setup. In the Methods section, we discuss an alternative method to determine the upper bound for P_{int}, which is independent of the measurement of a, but still results in a similar upper bound.

Despite the uncertainty in the specific value of P_{int}, the results acquired from the two independent experiments agree remarkably well. We conclude that, in the absence of all other energy-relaxation mechanisms, the ionizing radiation limits the qubit coherence to $\Gamma_1 \approx 1/4\,\text{ms}^{-1}$. In turn, shielding the qubits from environmental ionizing radiation improved their coherence. The observed energy relaxation rate was reduced by $\Gamma_1 \approx 1/22.7\,\text{ms}^{-1}$, instead of a complete reduction by the value $1/4\,\text{ms}^{-1}$ predicted in the absence of internal radiation, due to both the presence of internal radiation P_{int} in the actual experiment and the imperfect efficiency of the shield.

Discussion

The first reported results of the systematic operation of superconducting transmon qubits under intentionally elevated levels of ionizing radiation clearly show a deleterious effect on the performance of the qubits. We quantitatively determined the impact of radiation power density on the qubit coherence. It was found that shielding the qubits from naturally occurring radiation in the laboratory enhances their performance. A simple model of the ionization generation of quasiparticles suggests that transmon qubits of this design will need to be shielded against ionizing radiation in order to reach coherence times in the millisecond regime.

Future experiments can provide a more detailed understanding of the micro-physical mechanisms by which ionizing radiation specifically affects superconducting quantum devices through suitable choices of device designs, and appropriate choices of ionizing radiation sources. Practical approaches to mitigation schemes include a combination of careful selection of materials in the immediate vicinity of the qubit and adequate shielding against external gamma radiation to significantly reduce the impact of ionizing radiation on superconducting qubits. Such programs and strategies are readily employed in the development and installation of deep underground, highly shielded dark matter and neutrino research physics experiments[25,27–32]. In an analogous fashion, locating qubit systems deep underground where cosmic rays and cosmogenic activation are drastically reduced could provide benefits for advancing quantum computing research. Natural impurities in the substrate material, such as the radioactive ^{32}Si present in silicon[33], represent an otherwise irreducible limit on coherence times due to ionizing radiation without advanced purification methods (See Fig. 3b). These issues will need to be considered in the development of a robust, fault-tolerant quantum computer.

References

1. DiVincenzo, D. The physical implementation of quantum computation. *Fortschritte der Physik* **48**, 771–783 (2000).
2. Arute, F. *et al.* Quantum supremacy using a programmable superconducting processor. *Nature* **574**, 505–510 (2019).
3. Kandala, A. *et al.* Error mitigation extends the computational reach of a noisy quantum processor. *Nature* **567**, 491–495, DOI: 10.1038/s41586-019-1040-7 (2019).
4. Lutchyn, R., Glazman, L. & Larkin, A. Kinetics of the superconducting charge qubit in the presence of a quasiparticle. *Phys. Rev. B* **74**, 064515 (2006).
5. Jin, X. *et al.* Thermal and residual excited-state population in a 3d transmon qubit. *Phys. review letters* **114**, 240501 (2015).
6. Martinis, J. M., Ansmann, M. & Aumentado, J. Energy decay in superconducting josephson-junction qubits from nonequilibrium quasiparticle excitations. *Phys. review letters* **103**, 097002 (2009).
7. Serniak, K. *et al.* Hot nonequilibrium quasiparticles in transmon qubits. *Phys. Rev. Lett.* **121**, 157701 (2018).
8. Aumentado, J., Keller, M. W., Martinis, J. M. & Devoret, M. H. Nonequilibrium quasiparticles and 2 e periodicity in single-cooper-pair transistors. *Phys. review letters* **92**, 066802 (2004).
9. Taupin, M., Khaymovich, I., Meschke, M., Mel'nikov, A. & Pekola, J. Tunable quasiparticle trapping in meissner and vortex states of mesoscopic superconductors. *Nat. communications* **7**, 10977 (2016).
10. Serniak, K. *et al.* Direct dispersive monitoring of charge parity in offset-charge-sensitive transmons. *arXiv preprint arXiv:1903.00113* (2019).
11. Córcoles, A. D. *et al.* Protecting superconducting qubits from radiation. *Appl. Phys. Lett.* **99**, 181906 (2011).
12. Barends, R. *et al.* Minimizing quasiparticle generation from stray infrared light in superconducting quantum circuits. *Appl. Phys. Lett.* **99**, 113507 (2011).
13. Nakamura, Y., Pashkin, Y. A. & Tsai, J. S. Coherent control of macroscopic quantum states in a single-cooper-pair box. *nature* **398**, 786–788 (1999).
14. Oliver, W. D. & Welander, P. B. Materials in superconducting quantum bits. *MRS Bull.* **38**, 816–825 (2013).

15. Kjaergaard, M. *et al.* Superconducting qubits: Current state of play. *Annu. Rev. Condens. Matter Phys.* **11**, null, DOI: 10.1146/annurev-conmatphys-031119-050605 (2020). https://doi.org/10.1146/annurev-conmatphys-031119-050605.

16. Gottesman, D. Theory of fault-tolerant quantum computation. *Phys. Rev. A* **57**, 127–137, DOI: 10.1103/PhysRevA.57.127 (1998).

17. Grünhaupt, L. *et al.* Loss mechanisms and quasiparticle dynamics in superconducting microwave resonators made of thin-film granular aluminum. *Phys. Rev. Lett.* **121**, 117001 (2018).

18. Albrecht, S. *et al.* Transport signatures of quasiparticle poisoning in a majorana island. *Phys. review letters* **118**, 137701 (2017).

19. Koch, J. *et al.* Charge insensitive qubit design derived from the cooper pair box. *Phys. Rev. A* **76**, 042319, DOI: 10.1103/PhysRevA.76.042319 (2007).

20. Krantz, P. *et al.* A quantum engineer's guide to superconducting qubits. *Appl. Phys. Rev.* **6**, 021318 (2019).

21. Klimov, P. *et al.* Fluctuations of energy-relaxation times in superconducting qubits. *Phys. review letters* **121**, 090502 (2018).

22. Wang, C. *et al.* Measurement and control of quasiparticle dynamics in a superconducting qubit. *Nat. communications* **5**, 5836 (2014).

23. Allison, J. *et al.* Geant4 developments and applications. *IEEE Transactions on Nucl. Sci.* **53**, 270–278, DOI: 10.1109/TNS.2006.869826 (2006).

24. Agostinelli, S. *et al.* Geant4 — a simulation toolkit. *Nucl. Instruments Methods A* **506**, 250–303, DOI: https://doi.org/10.1016/S0168-9002(03)01368-8 (2003).

25. Aguilar-Arevalo, A. *et al.* Search for low-mass WIMPs in a 0.6 kg day exposure of the DAMIC experiment at SNOLAB. *Phys. Rev. D* **94**, 082006, DOI: 10.1103/PhysRevD.94.082006 (2016). 1607.07410.

26. Dicke, R. The measurement of thermal radiation at microwave frequencies. *Rev. Sci. Instruments* **17**, 268–275 (1946).

27. Agnese, R. *et al.* Projected sensitivity of the SuperCDMS SNOLAB experiment. *Phys. Rev. D* **95**, 082002, DOI: 10.1103/PhysRevD.95.082002 (2017).

28. Alduino, C. *et al.* First Results from CUORE: A Search for Lepton Number Violation via $0\nu\beta\beta$ Decay of ^{130}Te. *Phys. Rev. Lett.* **120**, 132501, DOI: 10.1103/PhysRevLett.120.132501 (2018).

29. Agostini, M. *et al.* Improved Limit on Neutrinoless Double-β Decay of ^{76}Ge from GERDA Phase II. *Phys. Rev. Lett.* **120**, 132503, DOI: 10.1103/PhysRevLett.120.132503 (2018).

30. Gando, A. *et al.* Search for Majorana Neutrinos Near the Inverted Mass Hierarchy Region with KamLAND-Zen. *Phys. Rev. Lett.* **117**, 082503, DOI: 10.1103/PhysRevLett.117.082503 (2016).

31. Aalseth, C. E. *et al.* Search for Neutrinoless Double-β Decay in ^{76}Ge with the Majorana Demonstrator. *Phys. Rev. Lett.* **120**, 132502, DOI: 10.1103/PhysRevLett.120.132502 (2018).

32. Albert, J. B. *et al.* Search for Neutrinoless Double-Beta Decay with the Upgraded EXO-200 Detector. *Phys. Rev. Lett.* **120**, 072701, DOI: 10.1103/PhysRevLett.120.072701 (2018).

33. Orrell, J., Arnquist, I., Bliss, M., Bunker, R. & Finch, Z. Naturally occurring ^{32}Si and low-background silicon dark matter detectors. *Astropart. Phys.* **99**, 9–20, DOI: 10.1016/j.astropartphys.2018.02.005 (2018). 1708.00110.

34. Hagmann, C., Lange, D. & Wright, D. Cosmic-ray shower generator (CRY) for Monte Carlo transport codes. In *2007 IEEE Nuclear Science Symposium Conference Record*, vol. 2, 1143–1146, DOI: 10.1109/NSSMIC.2007.4437209 (2007).

35. Mangiafico, S. S. Summary and analysis of extension program evaluation in R. *Rutgers Coop. Extension: New Brunswick, NJ, USA* (2016).

36. Wallraff, A. *et al.* Approaching unit visibility for control of a superconducting qubit with dispersive readout. *Phys. review letters* **95**, 060501 (2005).

37. de Visser, P. J. *et al.* Evidence of a nonequilibrium distribution of quasiparticles in the microwave response of a superconducting aluminum resonator. *Phys. Rev. Lett.* **112**, 047004, DOI: 10.1103/PhysRevLett.112.047004 (2014).

38. Goldie, D. J. & Withington, S. Non-equilibrium superconductivity in quantum-sensing superconducting resonators. *Supercond. Sci. Technol* **26**, 15004–15014, DOI: 10.1088/0953-2048/26/1/015004 (2013).

39. Barends, R. *et al.* Quasiparticle relaxation in optically excited high-q superconducting resonators. *Phys. Rev. Lett.* **100**, 257002, DOI: 10.1103/PhysRevLett.100.257002 (2008).

Acknowledgements

The authors thank Mitchell S. Galanek and Ami Greene (both of MIT) for assistance in oversight of radiation source use in the laboratory of the Engineering Quantum Systems (EQuS) group at MIT. The authors thank Michael R. Ames and Thomas I. Bork at the MIT Reactor (MITR) for production of the ^{64}Cu source through neutron activation at MITR and Ryan Samz for assistance in installing the source. The authors thank Mital A. Zalavadia (Pacific Northwest National Laboratory) for providing the compact $3'' \times 3''$ NaI detector used to measure the ambient levels of gamma-ray radiation present in the MIT laboratory where the radiation tests on the qubits were

performed. We thank Greg Calusine, Kyle Serniak, and Uwe von Luepke for designing and pre-characterizing the qubit samples. We thank Grecia Castelazo for help in operating the lead shield and Roni Winik for useful discussions.

This work was supported in part by the U.S. Department of Energy Office of Nuclear Physics under an initiative in Quantum Information Science research (Contract award # DE-SC0019295, DUNS: 001425594); by the U.S. Army Research Office (ARO) Grant W911NF-14-1-0682; by the ARO Multi-University Research Initiative W911NF-18-1-0218; by the National Science Foundation Grant PHY-1720311; and by the Assistant Secretary of Defense for Research and Engineering via MIT Lincoln Laboratory under Air Force Contract No. FA8721-05-C-0002. A.K. acknowledges support from the NSF Graduate Research Fellowship program. Pacific Northwest National Laboratory is operated by Battelle Memorial Institute under Contract No. DE-AC05-76RL01830 for the U.S. Department of Energy.

Author contributions statement

The following measurement was a collaboration between experts in quantum systems (A.P.V., A.H.K., F.V., S.G., and W.D.O.) and nuclear physics (J.A.F., J.L.O., B.A.V., B.L., and A.S.D). Simulations of background radiation and the impact of the radiation shielding were performed by A.S.D. and B.L and J.L.O. D.K., A.M., B.L., and J.Y. fabricated the qubit chips. The qubit experiment and data analysis were performed by A.P.V. and A.H.K. All authors contributed to writing and editing of the Letter.

Competing interests

The authors declare no competing interests.

Data Availability

The data that support the findings of this study are available from the corresponding author upon reasonable request and with the permission of the US Government sponsors who funded the work.

Code Availability

The code used for the analyses is available from the corresponding author upon reasonable request and with the permission of the US Government sponsors who funded the work.

Correspondence and requests for materials should be addressed to A.P.V and J.L.O.

Methods

Production of ^{64}Cu source

The ^{64}Cu radiation source was created by neutron activation of natural copper via the capture process ^{63}Cu (n,γ)^{64}Cu. Given its 12.7 hour half-life, ^{64}Cu is well suited for deployment in a dilution refrigerator, since it takes 72–100 hours to cool to base operating temperature. The irradiation took into account the anticipated ^{64}Cu decay during the cool-down period, by specifically irradiating at higher levels of ^{64}Cu than used in the qubit study and then allowing the foils time to decay to lower levels of activity.

Two copper disks created from the same McMaster-Carr foil were irradiated with neutrons at the MIT Reactor (MITR). The two foils are referred to as sample "A" and "A-Ref". The irradiated sample "A" was installed in the dilution refrigerator with the two qubits described in this study, while "A-Ref" was kept to determine the level of radioactive activation products. Each of the foils were 7.5 mm in diameter and 0.5 ± 0.1 mm thick and having a mass of 178.5 mg and 177.6 mg, respectively. The total neutron irradiation exposure was 7 minutes and 14 seconds in duration. Using a high purity gamma-ray spectrometer, the "A-Ref" sample was used to determine the ^{64}Cu activation level. We determine the activity of sample "A" to be (162 ± 2) μCi at 9:00 AM ET May 13, 2019. This activity is based on measurements of ^{64}Cu's 1346 keV gamma-ray.

Despite the high copper purity (99.99%), trace elements with high neutron cross-sections can also be activated from the neutron irradiation process. The same HPGe counter was used to determine the presence of other trace elements, the results of which are reported in Table 1.

Isotope	Half-life	nCi	$\pm$ %
^{65}Zn	244 d	0.042	10%
^{75}Se	120 d	0.006	50%
^{110m}Ag	250 d	0.062	4%
^{122}Sb	2.724 d	0.022	32%
^{124}Sb	60 d	0.014	11%
^{198}Au	2.697 d	0.497	2%

Table 1. Isotopes measured to be present in the sample "A-Ref" and the activity inferred for each in sample "A" as of May 24, 2019 at 4:00 PM Eastern time zone.

Radiation transport simulations and normalization

To estimate the power density imparted into the qubits by radiation, we developed a radiation transport simulation. The simulation was performed using the Geant4 toolkit[24] which is designed for modeling the interaction of radiation and particles with matter. The simulation geometry included a detailed model of the layers of the Leiden cryogenics CF-CS81 dilution refrigerator, the mounting fixtures and containment for the qubit, and the activated copper foil as it was located for the experiment. The qubit chip is modelled as a 380 μm thick piece of silicon with a 200 nm aluminum cladding. Input power density is estimated by measuring simulated energy deposited into the aluminum layer. Three separate radiation source terms are considered: ^{64}Cu and the other isotopes in the activated copper foil, naturally occurring background radiation primarily from the concrete walls of the laboratory, and cosmic ray muons.

To estimate the effect of isotopes in the copper, we make use of Geant4's radioactive decay simulation capabilities. Instances of each isotope are distributed uniformly throughout the simulated foil volume. Geant4 samples the available decay modes for that isotope with appropriate branching fractions, and generates the corresponding secondary particles (gammas, betas, positrons, etc), which are then tracked until they have deposited all their energy. By tallying up these events, we can estimate the average input energy density into the qubit substrate per decay, or equivalently the average power density per unit of isotope activity. The total simulated spectrum at various times during the qubit measurement campaign are shown in Fig. 3b.

To understand the background ionizing radiation levels present in the MIT laboratory where all qubit devices are operated, a $3'' \times 3''$ NaI scintillator detector was deployed near the dilution refrigerator where the qubit measurements described in this report were made. The detector was represented in the radiation transport simulation as a bare NaI cylinder (not including any housing, photomultiplier tube, etc). Gammas with an energy spectrum following the equilibrium emissions of the most common radioactive isotopes (^{238}U, ^{232}Th, and ^{40}K) are simulated starting in a sphere surrounding the NaI detector with an isotropic initial direction. A small number of simulations were run with different-sized initial locations to evaluate the impact of this parameter, yielding a 10% systematic uncertainty.

In order to fit to the measured data, the simulated energy deposits must be "smeared" to account for the detector's finite energy resolution. We used a quadratic energy scaling function to map energy to measured ADC counts, and a quadratic resolution function as a function of energy:

$$\sigma^2 = \sigma_0^2 + \sigma_1^2 E + \sigma_2^2 E^2 \tag{7}$$

Each of the energy scale and resolution coefficients is left free in the fit, as well as the flux of each isotope, for a total of 9 free parameters. The result for a fit over the range 0.2 - 2.9 MeV is show in Fig. 3a. The fit is much better when performed over a narrower region of the data. This could be improved with a more sophisticated response function, but we address the issue by performing the fit separately over three energy ranges: 0.2-1.3 MeV, 1.3-2.9 MeV, and 0.2-2.9 MeV, and taking the difference as a systematic uncertainty. This result is reported in the first line of Table 2. In total the uncertainty in the fits contributes 8% to the systematic uncertainty. The simulated energy deposition efficiency for each external isotope is approximately equal to 0.04 keV/s/mm^3 per cm^{-2}s^{-1}, which yields a total power density from environmental gammas of

0.060 ± 0.005 keV/s/mm^3.

The same NaI detector, operated at lower gain, is used to estimate the cosmic ray flux. Cosmic ray muons are simulated in a 1 m square plane above the detector, using the CRY package to generate the energy spectrum and angular distribution[34]. The muon flux taken directly from CRY is $1.24 \times 10^{-2}\mathrm{cm}^{-2}\mathrm{s}^{-1}$. A fit to the low-gain NaI data, using the same convolutional technique as for gammas, yields $(9.7 \pm 0.1) \times 10^{-3}\mathrm{cm}^{-2}\mathrm{s}^{-1}$, or about 20% lower than the CRY value. The same simulation gives an energy deposition efficiency in the qubits of (4.3 ± 0.2) keV/s/mm^3 per cm^{-2}s^{-1} of cosmic ray muon flux. This, in turn, yields a cosmic-ray induced power density of (0.042 ± 0.002) keV/s/mm^3.

In addition to depositing energy in the thin aluminum film, radiation will also interact and deposit energy in the silicon substrate. How much of this energy, if any, reaches the aluminum layer and is converted to quasiparticles is unknown, and we have therefore neglected this term in this analysis. Overall the ionization density is approximately the same for both materials, but some sources, in particular ^{64}Cu, deposit more energy into the aluminum than the silicon because a larger fraction of the total energy is emitted as betas. If the quasiparticle density is dominated by energy from the silicon rather than the aluminum, the relative strength of ^{64}Cu to the other trace activated isotopes would be approximately 60% lower. The external power density induced from environmental gammas is approximately 20% lower, while the cosmic ray power density is 13% higher, for a net 7% total increase in external power. The lead shielding effectiveness (η) is also approximately 15% higher for the silicon than aluminum.

Estimating the internal radiation rate P_{int}

An accurate estimate of the internal radiation rate P_{int} is important for comparing the feasibility of the shielding effect of the lead shield to the estimated effect of the external radiation power density on the qubit coherence $\delta\Gamma$ extracted from the ^{64}Cu experiment. A simple way for making the estimate is to extract it from the fit to the data in Fig. 3c). However, the accuracy of the estimate is relatively low since it is difficult to separate P_{int} from the coherence time of the qubit due to sources other than quasiparticles, Γ_{other}. In principle, it is possible to distinguish the two sources, because according to Eq. (4) the scaling of Γ_1 is proportional to $\sqrt{P_{\mathrm{ext}} + P_{\mathrm{int}} + P_{\mathrm{src}}}$ whereas the internal decoherence rate Γ_{other} adds up linearly to Γ_1, see Eq. (2). In practice, this is quite inaccurate, especially if quasiparticle loss is not the dominating loss-mechanism.

Instead, we employ the shielding experiment to calculate an upper bound for P_{int}. In the limit of $P_{\mathrm{int}} \gg P_{\mathrm{ext}}$, we can calculate an asymmetry parameter for the coherence times in the shield up or down positions,

$$A_i = 2\frac{\Gamma_1^{\mathrm{d},i} - \Gamma_1^{\mathrm{u},i}}{\Gamma_1^{\mathrm{d},i} + \Gamma_1^{\mathrm{u},i}} \approx \frac{\eta^{\mathrm{u}} - \eta^{\mathrm{d}}}{2} \frac{P_{\mathrm{ext}}}{P_{\mathrm{int}} + \frac{\Gamma_{\mathrm{other}}}{a\sqrt{\varpi_{\mathrm{q}}}}}, \tag{8}$$

where the index i refers to different rounds of the shield up/down experiment. The internal radiation rate P_{int} can be estimated using the experimentally measured median asymmetry parameter as

$$\tilde{P}_{\mathrm{int}} \approx \frac{(\eta^{\mathrm{u}} - \eta^{\mathrm{d}})}{2\langle A \rangle} P_{\mathrm{ext}} = 7.9\,\mathrm{keV\,mm^{-3}\,s^{-1}}, \tag{9}$$

where $\tilde{P}_{\mathrm{int}} = P_{\mathrm{int}} + \frac{\Gamma_{\mathrm{other}}}{a\sqrt{\varpi_q}}$. This gives the upper bound for P_{int}. Due to the other relaxation mechanisms, the actual value of P_{int} is lower. For example, $\Gamma_{\mathrm{other}} = 1/200\,\mu\mathrm{s}^{-1}$ would yield $P_{\mathrm{int}} \approx 1.6\,\mathrm{keV\,mm^{-3}\,s^{-1}}$ for the parameters of Q1. Here we emphasize that the estimate of the asymmetry parameter is based on the data gathered on all the seven qubits employed in the lead shield experiment, with all the qubits having different (fluctuating) values of Γ_{other}.

Efficiency of the lead shield

The reduction factor of external gamma-induced backgrounds by the lead shield was evaluated using the radiation transport simulation described previously. Gammas following the equilibrium emission spectra for ^{238}U, ^{232}Th, and ^{40}K were thrown isotropically from a 2.4 m sphere centered on the qubits, and the fraction of flux Φ reaching a smaller 8.5 cm sphere (fully inside the DR) was recorded. Table 2 shows the results for the no shield, shield down, and shield up, as well as the individual shield efficiency values $\eta^{\mathrm{u}} = 1 - (\Phi^{\mathrm{u}}/\Phi^{\mathrm{noshield}})$ and $\eta^{\mathrm{d}} = 1 - (\Phi^{\mathrm{d}}/\Phi^{\mathrm{noshield}})$.

To validate the simulations, the NaI detector was operated separately inside the lead shield at approximately the location of the qubits in the shield-up configuration. This configuration was also simulated, and the output fit to the measured spectrum using the same fit procedure as for the bare NaI. If the simulation and fit procedure are accurate, both fits should give the same values for the input flux. The results are reported in the first rows of Table 2. The results for U and Th are consistent, while the values for K differ by about 2.5σ. It may be that the lead itself has a high level of ^{40}K, but we treat this as a systematic uncertainty, which is $\sim 7\%$ of the total gamma flux.

Statistical analysis of the lead shield experiment

Since there are significant fluctuations in the internal energy relaxation rates Γ_{other} of the qubits, we performed a careful A/B test to verify that the effect of the lead shield on the qubit coherence was not due to statistical error. In the measurement of the energy relaxation rates of the qubits, there is uncertainty both due to the measurement accuracy and the fluctuations and drifts in the energy relaxation rates over time. To reduce the uncertainty due to the measurement accuracy, we measured the energy relaxation rates N times in each step of the A/B test. After N measurements the status of the lead shield was changed and we performed N more measurements. This cycle was repeated 65 times with a sample containing qubits Q1 and Q2. To speed up data acquisition, after that we installed a new sample with 6 qubits, of which 5 were used in the experiment, for which the measurement cycle was repeated 85 times. For

Isotope	K	Th	U
Lab flux ($\mathbf{cm^{-2}s^{-1}}$)			
bare fit	2.8 ± 0.1	2.7 ± 0.6	1.3 ± 0.1
shielded fit	3.3 ± 0.2	2.7 ± 0.8	1.3 ± 0.02
difference	-0.5 ± 0.2	0.1 ± 1	-0.01 ± 0.2
Flux fraction reaching qubit			
no shield	0.1232	0.1014	0.1003
shield down	0.1181	0.0978	0.0968
shield up	0.0284	0.0214	0.0208
η^{d}	0.041	0.036	0.035
η^{u}	0.769	0.789	0.793

Average shield efficiency

	η^{d}	η^{u}
external gammas	0.038 ± 0.007	0.781 ± 0.002
cosmic rays	–	0.02 ± 0.02
Total	0.022 ± 0.003	0.461 ± 0.001

Table 2. Statistics of simulations of environmental radiation sources in the laboratory environment. The background gamma flux is obtained by a fit to a measurement with a NaI scintillator (Fig. 3a), simulating and measuring both with and without the lead shield in the "up" position. Cosmic rays were also measured and simulated in both shield-off and shield-up conditions; the shield did not have a measurable effect in the "up" position, as expected; the effect is assumed to be zero in the "down" position. The "Average shield effienciency" values for η are weighted by each component's contribution to total external power. Statistical uncertainties on the fraction of flux reaching the interior of the DR are all 0.0001; uncertainties on η values for individual isotopes are all approximately 0.001.

the sample with qubits Q1 and Q2, $N = 50$, and for the sample with qubits Q3-Q7, $N = 10$.

Performing several short measurement cycles was crucial for reducing the uncertainty due to the slow drifts in the relaxation rates. The change in the energy relaxation rate $\delta\Gamma_1$ was calculated as the median of all the measured change in the energy relaxation rates. To estimate the average of $\delta\Gamma_1$ we used median in order not be sensitive to individual measurements where the energy relaxation rate fluctuated during a single cycle of the measurements. Additionally, we neglected all the data points where either Γ_1^{u} or Γ_1^{d} was less than $1/30\,\mu\mathrm{s}^{-1}$ or their difference was more than 10 standard deviations of all the measured differences. We calculated the 95% confidence intervals for $\delta\Gamma_1$ using the normal approximation for the confidence interval of the sample median[35].

Wilcoxon signed-rank test can be used to determine if the mean of two matched samples differ. It is a non-parametric test and can be used for data that is not normally distributed. For $\delta\Gamma_1$ Wilcoxon signed-rank test gives p-value = 0.006 for the null hypothesis that the means of the energy relaxation rates with and without the shield are the same. Since p-value $\ll 0.05$ we can reject the null hypothesis and conclude that the shield reduces the energy-relaxation rate. See Supplementary information for additional information on the analysis.

Supplementary material

Measurement setup

Fig. 5 shows the measurement setup used to measure the coherence times of the qubits. The qubit control pulses are created using a Keysight PXI arbitrary waveform generator. The in-phase and quadrature pulses are up-converted to the qubit transition frequency in an IQ-mixer, which acts as a single side band mixer. The readout pulses are created similarly. The control and readout pulses are combined and sent to the sample through a single microwave line. There is a total of 60 dB attenuation in the line to reduce the thermal noise from the room temperature and the upper stages of the dilution refrigerator. In the control line there are eccosorb filters before and after the sample, which reduce the infrared radiation reaching the qubit. The control line is inductively coupled to readout resonators R1 and R2.

To reach to the qubit, the control pulses have to pass through the readout resonator which acts as a filter. By using sufficiently strong control pulses the qubits can still be excited in 25 ns.

The qubit state is determined using dispersive readout[36]. The dispersive readout is based on the resonator frequency slightly changing depending on the state of the qubit. The change can be detected by using a single measurement tone near the resonator resonance frequency, and measuring the transmitted signal in the microwave line. The measurement signal is boosted using a chain of amplifiers. The first amplifier employed is a traveling wave parametric amplifier (TWPA), which has a very low noise temperature and gain up to 30 dB. As all quantum limited amplifiers, the TWPA requires a pump tone, which is driven by a signal generator at the room temperature. The microwave line carrying the pump tone is attenuated by 50 dB and is 50 Ω terminated at 10 mK stage of the dilution refrigerator. The signal is further amplified by the LNF HEMT amplifier, which is thermally anchored to the 3 K stage of the refrigerator. At room temperature, there is a final pre-amplifier followed by a heterodyne detector. The down-converted in-phase and quadrature signals are digitized using a Keysight PXI digitizer, with a 500 MHz sampling rate. The signal is integrated into the internal FPGA of the digitizer to extract the occupation probability of the qubit being in a given state.

In the experiments, we used two samples with 2 qubits in the first one and 6 qubits in the second sample. Of these 8 qubits, 7 were employed in the experiments. Table 3 shows the relevant parameters of those qubits. The reported energy relaxation times are median values during the lead-shield experiment. The values for Q1 and Q2 differ from those reported for ^{64}Cu measurements due to their fluctuation over time.

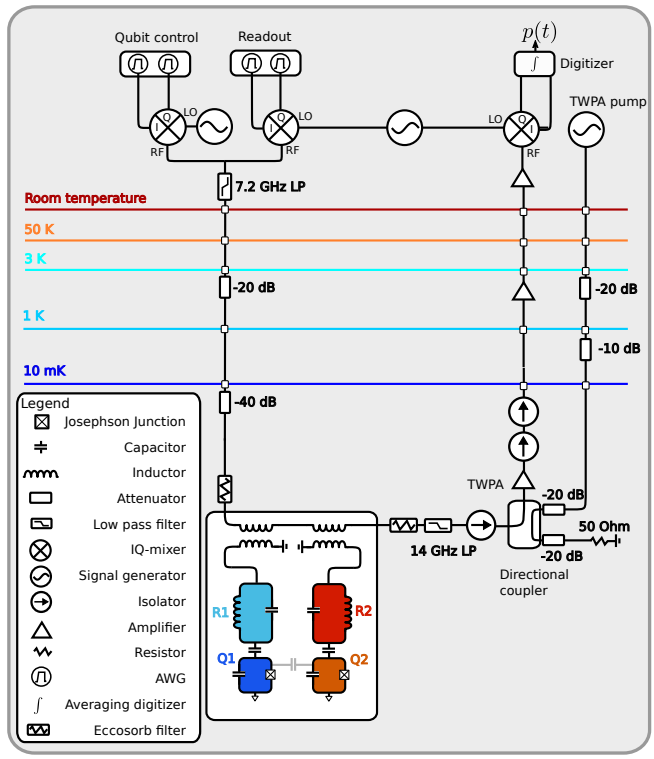

Figure 5. The setup used for measuring the coherence of the qubits. The diagram shows a simplified block diagram of the room temperature electronics used for measuring the coherence of the superconducting qubits.

Quasiparticle injection experiment

Quasiparticles can be injected into the circuit to study their relaxation dynamics. Here we attempt to determine whether the quasiparticle dynamics are dominated by the recombination

	$\omega_q/2\pi$ (GHz)	T_1 (µs)
Q1	3.48	50.4
Q2	4.60	45.0
Q3	3.00	76.8
Q4	3.09	71.8
Q5	3.16	61.8
Q6	3.26	69.4
Q7	3.33	72.8

Table 3. The parameters of the qubits used in the lead shield experiment.

rate r or trapping rate s, see Eq. (4) in the main text. In the absence of the external generation rate, the time evolution of the quasiparticle density can be solved from the differential equation in Eq. (4)[22],

$$x_{qp}(t) = \frac{x_{qp}(0)s}{-rx_{qp}(0) + e^{st}(s + rx_{qp}(0))}. \tag{10}$$

In the two limiting cases of no trapping or no recombination the time evolution can be simplified as

$$x_{qp}(t) = \frac{x_{qp}(0)}{1 + x_{qp}(0)rt} \tag{11}$$

or

$$x_{qp}(t) = x_{qp}(0)e^{-st}, \tag{12}$$

respectively.

Following the experimental protocol introduced in[22], quasiparticles can be generated by strongly driving the resonator coupled to Q1. The energy pumped into the resonator breaks Cooper pairs, resulting in elevated quasiparticle density. The generated quasi-particles gradually diffuse into the superconducting material around the resonator, including the qubit. We observed that a steady state in the quasiparticle density in the qubit was reached after $d_{qp} = 10\,\text{ms}$ of quasiparticle pumping, see Fig. 6a) for the pulse sequence. After the initial quasiparticle injection pulse, the quasiparticle density was estimated by measuring the qubit energy relaxation rate, see Eq. (3) in the main text. By changing the delay between the injection pulse and the energy relaxation rate measurement, we can determine the quasiparticle relaxation dynamics in our device, see Fig. 6b). We fitted the full model of Eq. (10) and found out that the quasiparticle trapping rate s was negligible, shown by the solid green line in Fig. 6b). The fit includes the internal relaxation rate of the qubit, $\Gamma_{other} \approx 1/35\,\mu\text{s}^{-1}$. The dash dotted orange line shows the fit using a model that only includes recombination. This line almost exactly matches the fit using the full model, confirming our assumption that recombination is the dominant quasiparticle decay process in our devices. The dotted orange line assumes no internal energy relaxation $\Gamma_{other} = 0$. Blue dash dotted line shows the model which assumes trapping as the only decay mechanism of quasiparticles. The dotted blue line shows the model without Γ_{other}. The model that assumes only trapping is strongly disfavored by the data.

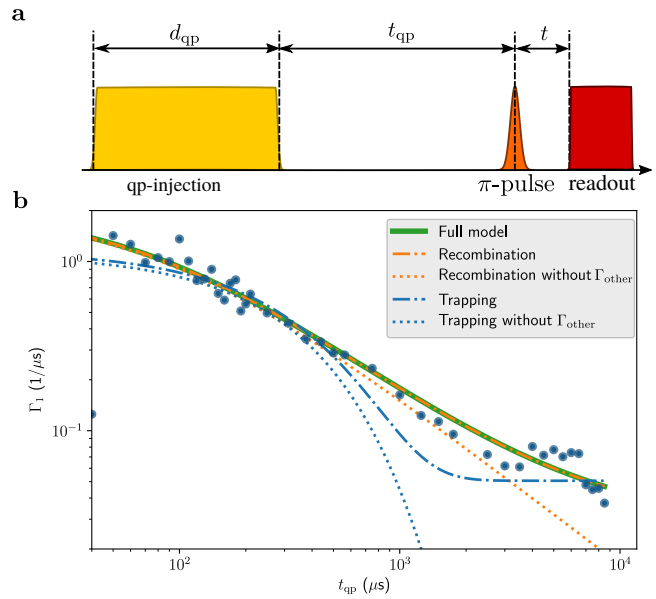

Figure 6. Quasiparticle injection experiment a) shows the pulse sequence in the quasiparticle injection experiment. First a strong microwave pulse is applied for the duration of d_{qp} to the resonator, which excites quasiparticles. After time t_{qp} the coherence time of the qubit is measured. b) shows the energy relaxation rate of the qubit Q1 during the quasiparticle injection experiment (blue dots). A solid green line shows a fit to the data using the full model that includes quasiparticle trapping and recombination. Orange dash dotted line shows the model with only recombination, dotted line shows the same model without the internal quasiparticle relaxation rate Γ_{other}. Blue dash dotted line shows the fit to the model that only includes trapping of quasiparticles. Dotted blue line shows the trapping model without Γ_{other}.

Resonator measurements

Each qubit on the device is addressed and operated via a separate resonator using a microwave probe pulse in the resonator dispersive regime. To experimentally determine the resonant response frequency of the resonator, we scan the probe frequency at different powers, seeking resonance response. In the high power regime, the resonator becomes effectively decoupled from the qubit, therefore to effectively measure the qubit and its interaction with the resonator we operate the resonator in the dispersive power regime. We systematically repeat this frequency and power scan at different source radiation intestines to study the behavior of our resonators in the presence of ionizing radiation.

When exposed to ionizing radiation, the resonators become

unstable and exhibit random fluctuations in their resonance frequency. As the radiation intensity decreases with time, the fluctuation decreases until the resonator is stable once again (Fig. 7**a)-d)**). This behavior is consistent with previous measurements of superconducting resonators in the presence of quasiparticles[37,38]. We monitor the resonator frequency and full-width-half-max (FWHM) through the duration of the experiment. We observe that as the radiation power decreases, both properties of the resonator fluctuations decrease until they converge to the value measured during our control experiment. Furthermore, the median of the resonator frequency shift ($\Delta\omega_r$) and the FWHM for our measurements follows an exponential decay as a function of time with a half-life of $t_{1/2} = (21.74 \pm 2.8)$h and $t_{1/2} = (24.16 \pm 0.78)$h respectively. The observed decay half-life values are very close to being twice the half-life of the ^{64}Cu source. This effect can be explained by quasiparticle induced change in the kinetic inductance of the resonator. The kinetic inductance of superconducting resonators is directly correlated with the number of quasiparticles[39]: $\delta L_k/L_k = \frac{1}{2}\delta n_{qp}/n_{qp}$. Furthermore, the change in the resonator frequency is directly proportional to the change in the kinetic inductance: $\delta\omega/\omega_0 = \frac{\alpha}{2}\delta L_k/L_k$. Therefore, $\delta\omega/\omega_0 \propto \delta n_{qp}/n_{qp}$. According to Eq. (5) in the main text, the quasiparticle density depends on the square root of radiation power, and therefore we expect the resonator frequency decay constant to be twice that of the radiation source.

Measurement of the qubit energy relaxation rate

At the beginning of the measurement, all the qubits are initialized in their ground states. Due to the finite temperature of their environment and hot quasiparticles[7], there is a small excited state population, approximately 1.7 % in all the qubits. This corresponds to an effective temperature $T_{\text{eff}} \approx 40\,\text{mK}$[5]. At this temperature, the thermal quasiparticle population can be estimated to be

$$x_{qp}^{\text{thermal}} = \sqrt{2\pi k_B T \Delta}\, e^{-\frac{\Delta}{k_B T_{\text{eff}}}} \approx 4 \times 10^{-24}. \tag{13}$$

The qubit energy relaxation rate Γ_1 is measured by first exciting the qubits to their first excited state using a microwave π-pulse, see Fig. 8a). The state of all the qubits is measured simultaneously after time t, which gives an estimate for their excited state population $p(t)$. By changing t, the time evolution of the populations can be determined, see Fig. 8b). The model described in Eq. (2) in the main text can be fitted to the measured data to find the energy-relaxation rate Γ_1 of the qubits.

Operation of NaI detector

A standard commercial NaI detector measures energy deposited in the NaI crystal through the scintillation light created when γ- or x-rays scatter atomic electrons in the crystal. The magnitude of the scintillation light signal, measured by a photomultiplier tube (PMT), is proportional to the energy deposited in the NaI crystal by the incident radiation. As

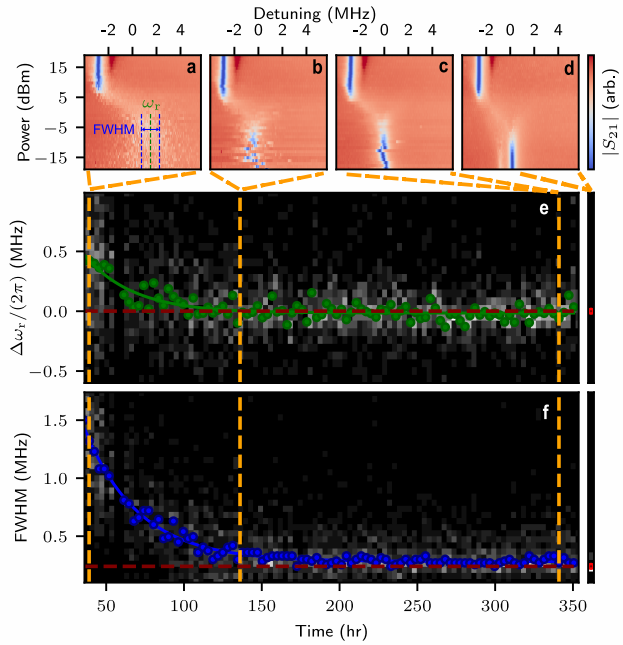

Figure 7. Resonator single-tone spectroscopy. **a)-d)** show the transmission profile of resonator 1 as as a function of readout power and readout frequency at different times throughout the experiment. When exposed to a high level of radiation, the resonator frequency becomes unstable in the dispersive regime which is used for reading out the qubit. The resonator becomes more stable as the radiation source decays. **e)** shows the change in the resonance frequency, $\Delta\omega_r$, due to radiation through out the experiment. We observe that the median $\Delta\omega_r$ follows an exponential decay with a half-life of $t_{1/2} = (21.74 \pm 2.8)$h. Furthermore, in **f)** we see the full-width-half-max (FWHM) of the resonator also exponentially decay with a half-life of $t_{1/2} = (24.16 \pm 0.78)$h until converging to the control value.

the specific energy of γ- or x-rays are indicative of the radioactively decaying nucleus, an energy spectrum measured by the NaI detector can be used to determine the relative contributions of ionizing radiation in the laboratory due to different naturally occurring radioactive isotopes. In a normal laboratory environment, the dominant naturally occurring radioactive nuclei consist of isotopes in the uranium (^{238}U) and thorium (^{232}Th) decay chains as well as ^{40}K. These features are identified in Fig. 3a).

It is possible to reduce the high voltage applied to the PMT, effectively reducing the gain on the scintillation light signal from the NaI detector, allowing for the measurement of ionizing cosmic rays passing through the NaI crystal. In this case, muons pass through the NaI crystal generating ionization along the entire path length. At the high energies of cosmic ray secondary muons, they pass through the crystal largely as a minimum ionizing particle. Thus, the flux of cosmic rays passing through the NaI crystal is determined mainly by

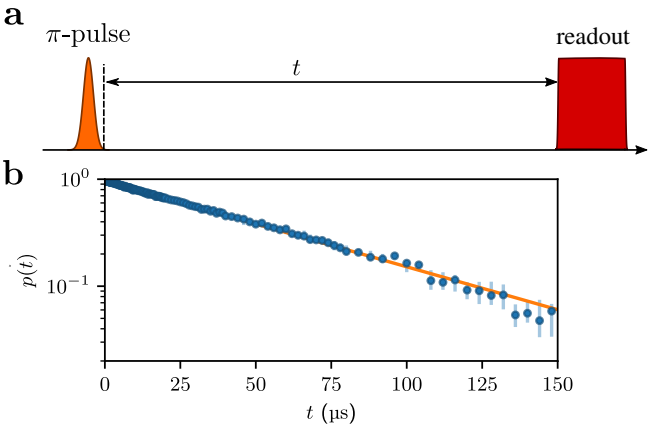

Figure 8. Energy relaxation rate measurement of the qubits a) shows the pulse sequence used to measure the energy relaxation rate of all the qubits. First a π pulse is applied to all the qubits. After time t a measurement pulse is used to determine the state of the qubits. b) The qubit excited state population relaxes exponentially as a function of time. Blue circles show the measured qubit excited state populations and the orange line is an exponential fit using the model of Eq. (2).

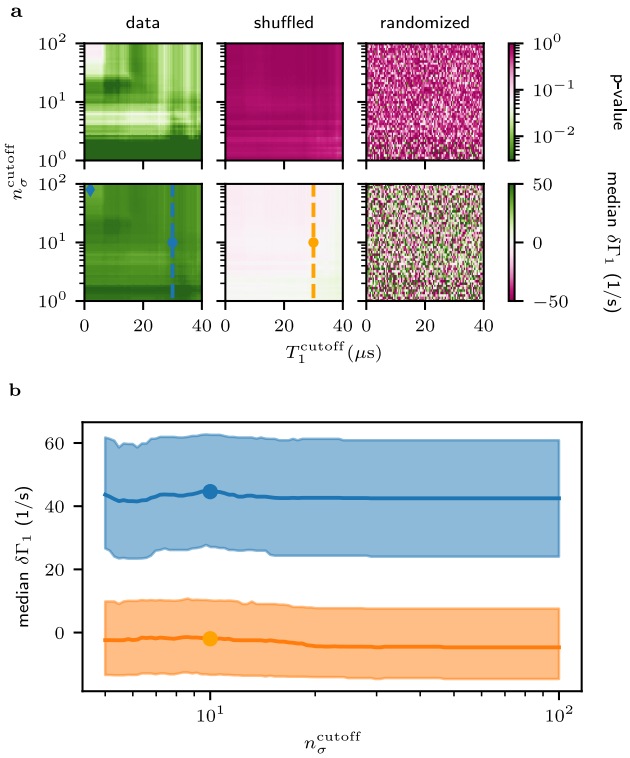

Figure 9. The effect of post-processing on the lead shield effect A/B test a) The upper row shows the p-value of the Wilcoxon signed rank test for three different test cases and for the different post-processing parameters. On the horizontal axis the T_1^{cutoff} is varied. The vertical axis shows the effect of applying a cutoff to the difference in the energy relaxation rates when the shield status is changed. The first column shows the actual data. The middle column shows a reference experiment, where the energy relaxation rates are compared without moving the shield. The last column shows the data when the energy relaxation rate pairs are randomized. The lower row shows the median of the effect of the shield on the energy relaxation rate $\delta\Gamma_1$. b) The median of $\delta\Gamma_1$ along the dashed lines in a). The filled area shows 68% confidence intervals for the median.

spectral features present above 2.7 MeV (see Fig. 3).

Additional information for the statistical analysis of the lead shield

We did several tests to verify that the effect of the lead shield $\delta\Gamma_1$ was not just a statistical fluctuation. First, we verified that the result is not sensitive to post-processing we did to the data. The first panel of Fig. 9a) shows the p-value of the Wilcoxon signed-rank test for a range of different cutoff parameters. The p-value stays low for all the sensible parameters we tested, verifying that the finding is not an artifact of post-processing. The median value is similarly insensitive to the post-processing, shown in the lower left panel. The blue diamond in the upper left corner shows the point where no post-processing is done. The blue circle shows the values which we use in the main text, $T_1^{\text{cutoff}} = 30\,\mu\text{s}$ and $n_\sigma^{\text{cutoff}} = 10$.

Next, we tried shuffling the data by comparing the energy relaxation rates of the measurements to the next measurement without moving the shield. In this case, we expected the signal to completely vanish. The result is shown in the middle column of Fig. 9a). In this case, the p-value is close to 1, which implies that we must accept the null-hypothesis that there is no signal, as expected.

In the third test, we completely randomized the pairs of measurements which we compare, resulting in overall high p-value, supporting our analysis (third column).

Fig. 9b) shows a cutoff of Fig. 9a) along the dashed lines in the left and middle panels. The filled areas show the 95 % confidence interval of the medians.

In Fig. 10 we show the histogram of all the measured asymmetry parameters, calculated according to Eq. (8) in the methods section. The median of the asymmetry is $\langle A \rangle \approx 0.0028$.

Finally, Fig. 11 shows the histogram of the measured T_1 times of all the qubits in the lead shield experiment. Their median energy relaxation rates are listed in Tab. 3. Fig. 12 shows the coherence times of all the qubits in the order in which they were measured. There are significant fluctuations and drift in the coherence times of all the qubits. However, by raising and lowering the shield often enough (every 50th measurement for qubits Q1 and Q2, and every 10th measurement for qubits Q3-Q7) the slow drift is mostly cancelled.

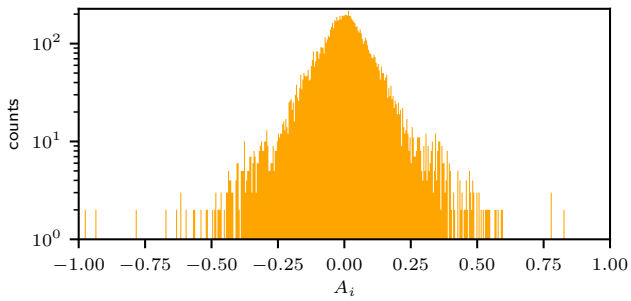

Figure 10. The asymmetry parameter The distribution of the asymmetry parameter $\langle A \rangle$ of the energy relaxation rates between the shield in up or down position.

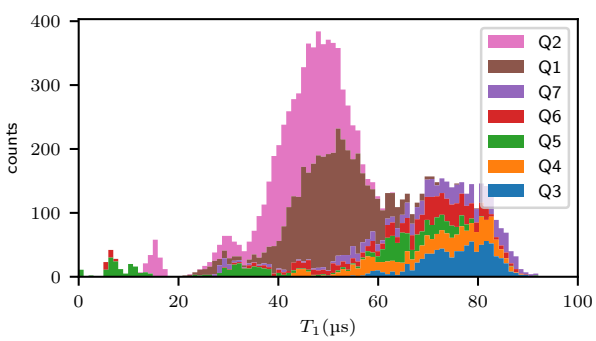

Figure 11. Stacked histogram of the combined lifetimes of all the qubits in the lead shield experiment.

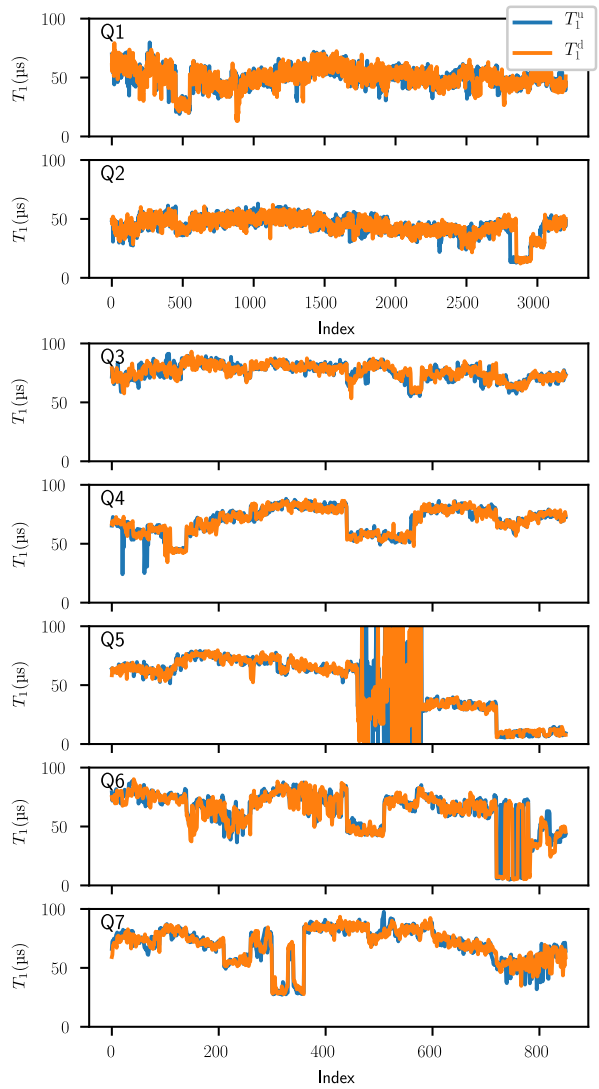

Figure 12. The coherence time distribution for qubits Q1-Q7 during the lead shield experiment while the shield is in up (blue) or down (orange) positions.